NEUROPHYSIOLOGY

An artificial remote tactile device with 3D depth-of-field sensation

Shanshan Zhu[1,2], Yuanheng Li[1,2], Huoerhute Yelemulati[1,2], Xinping Deng[1,2], Yongcheng Li[1,2], Jingjing Wang[3], Xiaojian Li[3,4], Guanglin Li[1,2]*, Paschalis Gkoupidenis[5]*, Yanlong Tai[1,2]*

Flexible tactile neuromorphic devices are becoming important as the impetus for the development of human-machine collaboration. However, accomplishing and further transcending human intelligence with artificial intelligence still confront many barriers. Here, we present a self-powered stretchable three-dimensional remote tactile device (3D-RTD) that performs the depth-of-field (DOF) sensation of external mechanical motions through a conductive-dielectric heterogeneous structure. The device can build a logic relationship precisely between DOF motions of an external active object and sensory potential signals of bipolar sign, frequency, amplitude, etc. The sensory mechanism is revealed on the basis of the electrostatic theory and multiphysics modeling, and the performance is verified via an artificial-biological hybrid system with micro/macroscale interaction. The feasibility of the 3D-RTD as an obstacle-avoidance patch for the blind is systematically demonstrated with a rat. This work paves the way for multimodal neuromorphic device that transcends the function of a biological one toward a new modality for brain-like intelligence.

INTRODUCTION

Biological sensorimotor systems are capable of acquiring and transmitting the external information to the inner nervous system in the form of electrochemical signals and then generating motor feedback to construct the interaction with the outside world (1). On this basis, emerging biomimetic devices are endowed with many functional similarities in respect to the biological counterparts and bridge the gap between artificial and biological systems by sharing common computational and processing primitives (2–6). Thereinto, biomimetic sensation is of great significance for human rehabilitation and novel artificial somatosensory systems with higher-order functionalities and multimodality. This venture is essential for the development of prosthetics (7), wearables (8), intelligence robots (9–12), and human-machine collaboration (HMC). Up to now, various artificial sensory systems have been developed that emulate the vision (13), hearing (14), touch (3), taste (15), and olfaction (16) of human beings, enabling us to perceive the surrounding environment by creating multisensory streams that are necessary to act upon the environment.

Of particular interest for the enhancement of the HMC are tactile electronics (6, 17–23). They mainly imitate the sensory functions of biological skin to external mechanical motions, including static recognition [the location or distribution of contact points (24), the size of contact area (19, 25), the surface topography of contact objects (3), etc.] and dynamic recognition [pressure in the vertical direction (4, 25, 26), slip or friction in the horizontal direction (27), etc.]. As for the mechanisms, they involve triboelectric effect (28, 29), piezoelectric/resistive/capacitive effect (3, 30), electrostatic induction (31), electromagnetic effect (32), or their combination. Nevertheless, this kind of sensation invariably stays at the level of two-dimensional (2D) skin surface with compulsive contact/pressure, which delivers incomplete information about the external environment and generates inevitable contact damage and power consumption (33). With regard to the perception in a 3D space without contact force, the traditional approaches involving techniques of laser (34), infrared (35), ultrasound (36), etc. (37), are adopted. However, their further application in HMC is restricted by disadvantages such as complex device layouts, hard-to-integrate properties, and high cost. Methods based on magnetism or humidity have also been explored, but they are still confined to special conditions of electromagnetic induction or limited sensing range within 1 cm (38, 39). Then, the noncontact sensors based on triboelectricity and electrostatic effects have been quickly developed, while the sensing surface generally needs to be precharged, and the working mechanism involves the complex superposition of multiple electric fields (40–42). The above restrictions like special applicable conditions, limited perceptual range, and inevitable precharged procedure hinder the further development of HMC, in both transcending the basic function of biological skin and deepening the integration of human and artificial intelligence (HI and AI, respectively) in a 3D environment (43).

Most objects in the environment like human body (44), natural hairs (45), or polymeric materials (46) are naturally charged due to their inevitable interactions with others. On the basis of this character and motivated by the need for augmenting the skin capabilities with previously unidentified modalities, we report a stretchable self-powered 3D remote tactile device (3D-RTD), which perceives the depth-of-field (DOF) mechanical motions of such external naturally charged object. This sensory device is composed of a conductive-dielectric heterogeneous structure [Au-ethylene-vinyl acetate (Au-EVA)], which imitates the signal transmission and connection of synaptic function (47) based on the electrostatic polarization and electron transfer. Thus, the virtual synapse 3D-RTD builds a corresponding logic relationship between proximity-separation motions of an active

[1]CAS Key Laboratory of Human-Machine Intelligence-Synergy Systems, Shenzhen Institute of Advanced Technology (SIAT), Chinese Academy of Sciences (CAS), and the SIAT Branch, Shenzhen Institute of Artificial Intelligence and Robotics for Society, Shenzhen 518055, China. [2]Guangdong-Hong Kong-Macao Joint Laboratory of Human-Machine Intelligence-Synergy Systems, SIAT, CAS, Shenzhen 518055, China. [3]CAS Key Laboratory of Brain Connectome and Manipulation, The Brain Cognition and Brain Disease Institute (BCBDI), SIAT, CAS, Shenzhen 518055, China. [4]Shenzhen-Hong Kong Institute of Brain Science-Shenzhen Fundamental Research Institutions, Shenzhen 518055, China. [5]Molecular Electronics Department, Max Planck Institute for Polymer Research, Ackermannweg 10, Mainz 55128, Germany.
*Corresponding author. Email: gl.li@siat.ac.cn (G.L.); gkoupidenis@mpip-mainz.mpg.de (P.G.); yl.tai@siat.ac.cn (Y.T.)

object and the generated potential signals. The source of sensation is analyzed on the basis of this heterogeneous structure, with COMSOL finite element analysis and dielectric constant regulation of sensory material. The feasibility of the 3D-RTD as a neural interface patch (48) is verified via constructing an artificial-biological hybrid system where 3D-RTD forms a 3D remote tactile system (3D-RTS), serving as an energy-autonomous sensory system to be assembled with a biological (rat) motor system. Accordingly, the target muscular contraction patterns of the rat are directly operated in response to DOF sensation. The augmented sensation and interaction of the 3D-RTD as a neural interface patch for the blind are demonstrated in an obstacle-avoidance scenario, with a rat walking in a dim environment to perceive potential collision, which cannot be achieved by conventional 2D sensors with indispensable contact. This demonstration highlights that the 3D-RTD has the ability of scene association and logical recognition and can be combined with biological perception, serving as a new modality for brain-like intelligence.

RESULTS
Remote tactile system with 3D DOF sensation
As representative of the human perceptual intelligence, biological tactile feedback starts with the sensation of a real skin being touched by an external object as shown in Fig. 1A. Specifically, the mechanical deformation of the skin at the contacting area induces the inferior tactile corpuscles to transfer the corresponding potential signals to the central nervous system and then triggers the sensory-motor neural circuits to achieve tactile feedback. On the basis of the similar signal transmission loop and principle, we propose a self-powered 3D-RTD and 3D-RTS with enhanced capabilities, in comparison to the biological counterpart with 2D sensation. As shown in Fig. 1B, the constructed sensorimotor system shows the synergetic operation of the biomimetic sensory and biological motor system. Specifically, the DOF mechanical motion of a hand triggers the 3D-RTD to yield sensory output through the virtual synapse, based on electrostatic polarization and electron transfer. Then, the resulted potential changes are delivered to actuate biological muscles, performing connection and communication between the artificial and the biological world.

A photograph of a typical 3D-RTD can be seen in Fig. 2A, which is composed of a double-layer structure of dielectric material and metal electrode. The dielectric layer is for sensation, being composed of flexible dielectric polymer EVA (thickness of 130 μm and diameter of 3 cm) and $BaTiO_3$ (BTO; average diameter of ~30 nm) nanoparticles uniformly distributed inside. The tensile performance meets the requirement of complying with skin deformation up to ~30% (fig. S4) (49, 50). The grounded conductive layer (thickness of ~30 nm) is assembled onto the EVA and used for electron transfer
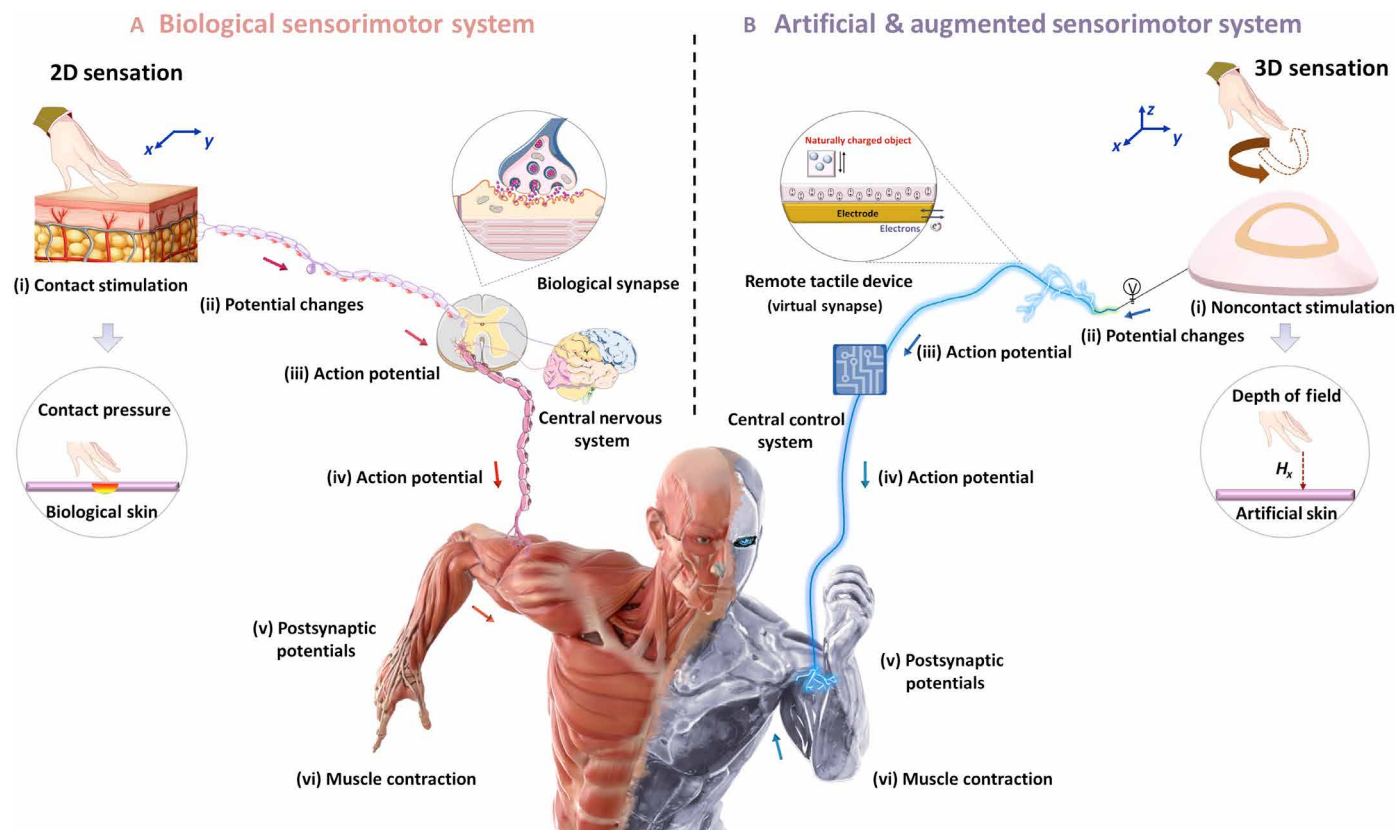

Fig. 1. Schematic illustration of biological and artificial sensorimotor system. (**A**) Biological sensorimotor system. (i to iii) When the contact stimulation is applied on the skin surface, excitatory potentials will be generated and travel along the sensory nerve and synapse to the spinal cord/brain. (iv to vi) Then, the action potentials are transported through the motor nerve and contribute to neuromuscular junction, thereby finally causing corresponding activity. (**B**) Artificial and augmented sensorimotor system. (i to iii) In the artificial 3D-RTS, a DOF mechanical stimulation triggers the 3D-RTD to generate sensory potential spikes via electrostatic polarization and electron transfer. (iv to vi) Then, the action potentials are transferred through the central integrated circuit to activate muscle contraction.
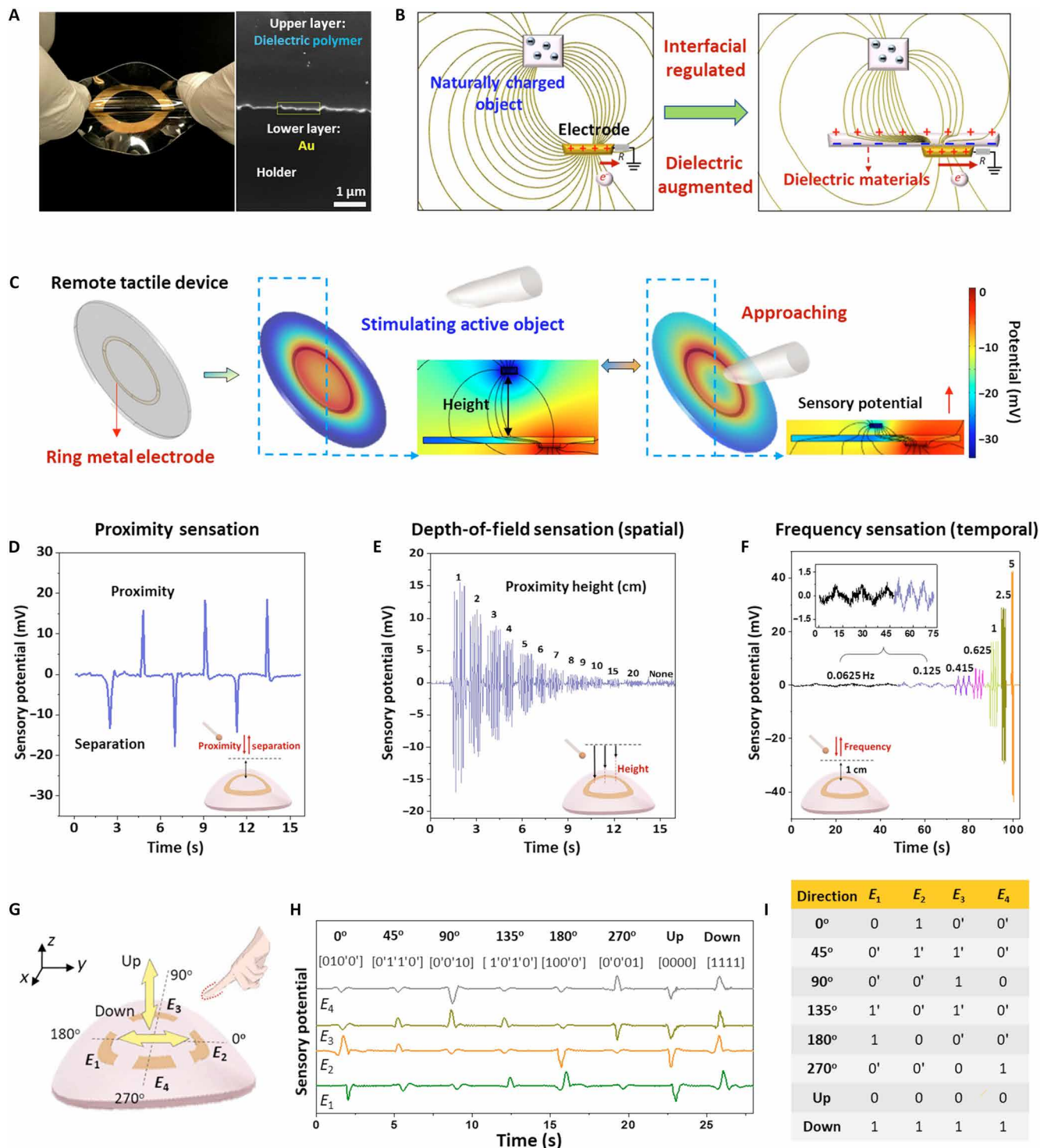
Direction	E_1	E_2	E_3	E_4
0º	0	1	0'	0'
45º	0'	1'	1'	0'
90º	0'	0'	1	0
135º	1'	0'	1'	0'
180º	1	0	0'	0'
270º	0'	0'	0	1
Up	0	0	0	0
Down	1	1	1	1

Fig. 2. Experimental and simulation results of the 3D-RTD. (**A**) Optical and scanning electron microscopy images of the flexible and stretchable self-powered 3D-RTD. (**B**) Illustration to show the working principle of 3D-RTD with the enhanced interaction between external naturally charged active object and the constructed conductive-dielectric heterogeneous structure. (**C**) Finite element simulation by COMSOL to present the variation of 3D electric field intensity and corresponding 2D electric field lines inside 3D-RTD when a charged active object is approaching or away. The relationship between the motion modes of the active object and the corresponding potential signals: (**D**) proximity-separation motion, (**E**) variable end heights, and (**F**) variable motion frequencies. Note that 3D-RTD is kept grounded via electrode during all tests unless otherwise specified. The total number of electric field lines in (C) COMSOL simulation is set as 15 to better present the variations for sensing. PVDF film with natural negative charges is used as the active object in all experiments, without electrical polarization. For (D) to (F), the active object moves in the direction perpendicular to the surface of the 3D-RTD, and the motion frequency represents the reciprocal of one-round motion time. (**G** to **I**) 3D sensing function and related encoding of 3D-RTD with four-channel electrodes, where [1]/[1'] denotes positive/weak positive signal and [0]/[0'] denotes negative/weak negative signal.

from/to the ground, which resulted from polarization and nearby charge induction. The conductive-dielectric heterogeneous structure is competent in sensation and transmission of external information, similar to a biosynapse. As for the sensing mechanism illustrated in Fig. 2B, when the metal electrode is around a charged active object, it will be polarized by the electric field generated by the charged one. Then, the polarization degree of the metal electrode changes with varying distances between the two parts, and the electric potential signals are generated when the electrode is grounded, driving the charge migration (51, 52). Furthermore, the sensory function based on electric field is enhanced through constructing the heterogeneous interface between the high dielectric material and metal electrode, because the dielectric has a high polarization response (53). Compared to the electrode-air heterogeneous interface, the electrode-dielectric one effectively converges the electric field lines and enhances the sensory performance (figs. S1 and 2). When the position of a freely active object changes, asymmetric charge distribution occurs on the surface of the dielectric layer due to the changed orientation of the electric dipoles inside, and then, electron transfer occurs in the conductive layer with nearby charge induction (fig. S6). On this basis, the external noncontact mechanical motion of an active object in a 3D space can be qualitatively and quantitatively characterized, by distinguishing the positive and negative potential peak features, the amplitude, and frequency of output signals. Accordingly, the induced electric field would be changed when the dielectric material is regulated, and the constitutive equation related to relative dielectric constant is shown below (section S1)

$$\Delta V = \frac{\sigma_d' S_d}{\varepsilon_0 \varepsilon_r} d = \left(E_0 - \frac{E_0}{\varepsilon_r} \right) S_d \cdot d \qquad (1)$$

where ΔV is the output potential, E_0 is the electric field intensity generated by a naturally charged object, σ_d' is the polarized surface charge density of the dielectric layer, ε_r is the relative dielectric constant, ε_0 is the absolute dielectric constant, and S_d and d are the area and thickness of the dielectric layer, separately. Thus, the sensory potential presents a proportional relationship with both the plane dimension and thickness of the dielectric layer (figs. S3 and S4), as well as the dimension and total amount of surface charges of the external objects (figs. S13 and S14). Results also show that no additional charging is required for the dielectric layer (fig. S5). Then, to improve the sensitivity of the device, the interfacial polarization of the dielectric layer responding to the electric field and the corresponding electron transfer in the conductive layer are enhanced by adding BTO nanoparticles via an increased dielectric constant (figs. S10 to S12) (54, 55).

3D remote tactile device

To visualize the sensory potential, finite element simulation based on COMSOL Multiphysics software package is used. In this way, the sensory capabilities of 3D-RTD to noncontact mechanical motion are qualitatively presented in Fig. 2C. Both 3D internal electric field intensity and corresponding 2D electric field lines demonstrate notable changes when a negative charged pointer (i.e., a finger) is approaching the surface of 3D-RTD, that is, stronger internal electric field and denser electric lines. As a consequence, the sensory potential increases accordingly until a new charge balance. On the contrary, the opposite potential signal appears when the finger moves away, where the charges move back immediately (movie S1).

Thus, a clear relationship is presented between the positive and negative amplitude of the potential signals and the direction and displacement of external mechanical motions.

The sensory capabilities of the proposed device are systematically characterized through diverse motion modes of an active object, in both temporal and spatial perspectives as shown in Fig. 2 (D to F). Note that, to avoid the interference from the active object, we use polyvinylidene difluoride (PVDF) film with natural negative charges to perform mechanical motions for all experiments (56). First, proximity-separation motion in the DOF direction of the active object can be logically perceived with the output as positive or negative sensory potential (V_{PER}) sign (Fig. 2D and figs. S16 and S17). When the object moves closer to the surface of 3D-RTD from the typical height of 10 to 1 cm, a positive V_{PER} of ~15 mV is obtained. On the contrary, a negative V_{PER} appears when the active object moves away, due to the opposite direction of electron-charge transfer (see COMSOL simulation in fig. S7). It should be noticed that both positive and negative sensory signals can be output instantaneously, with an average response time < 0.5 s and no recovery time.

The sensation to motion height is also investigated, named as spatial DOF sensation. As shown in Fig. 2E, when the object descends vertically from a fixed height of 21 cm to variable ends, the resulting V_{PER} is found to be closely related to the end height value. V_{PER} has an order of magnitude difference from ~15 to 1.5 mV as the motion end height ranges from 1 to 20 cm above the device surface, indicating a high spatial sensitivity. It is reasonable that the electrostatic polarization becomes weaker when two components move apart. Next, the temporal identification of the 3D-RTD is shown by performing periodic proximity-separation motion with variable frequencies of the active object (Fig. 2F). The profiles of sensory potential are directly related to motion frequency, with perceiving accuracy from 0.0625 to 5 Hz where the V_{PER} amplitude and peak number increase accordingly. The frequency of the sensory signals can track the frequency of the mechanical motion well, reflecting the high sensitivity of the proposed 3D-RTD. On the basis of these characters, devices with electrode from single channel to two channels (fig. S16) and then four channels (Fig. 2G) exhibit the sensing functions from uniaxial-1D to stereo-3D DOF. Through logic languages such as [0, 1], the sensation and recognition of motions at typical angles in both horizontal and vertical direction can be realized. In turn, motions at any angle can be calculated by the multiple sensory values. More complex gestures can also be recognized via systematic neural decoding, which we will not discuss in this work. Besides, the simultaneous energy harvest that is modulated by motion parameters shows the potential for further powering autonomous electronic devices or circuits (41, 57).

3D remote tactile system

To evaluate the capability of the artificial 3D-RTD as a virtual synapse in the function of connection, it is integrated with the skeletomuscular system of a rat, where the artificial system activates the muscle movement of the rat's hindlimb when 3D-RTD is triggered by the DOF motion of the active object. Two systems are proposed in Fig. 3A: (I) 3D-RTS and (II) stimulation and force measurement system (fig. S18). Specifically, the 3D-RTD in system I is located on the left back of the rat, and the real-time V_{PER} signals are generated when the active object is moving in DOF direction. On the basis of a specifically designed signal transmission mode (figs. S19 and S20), the positive and negative V_{PRE} could be recognized and exported
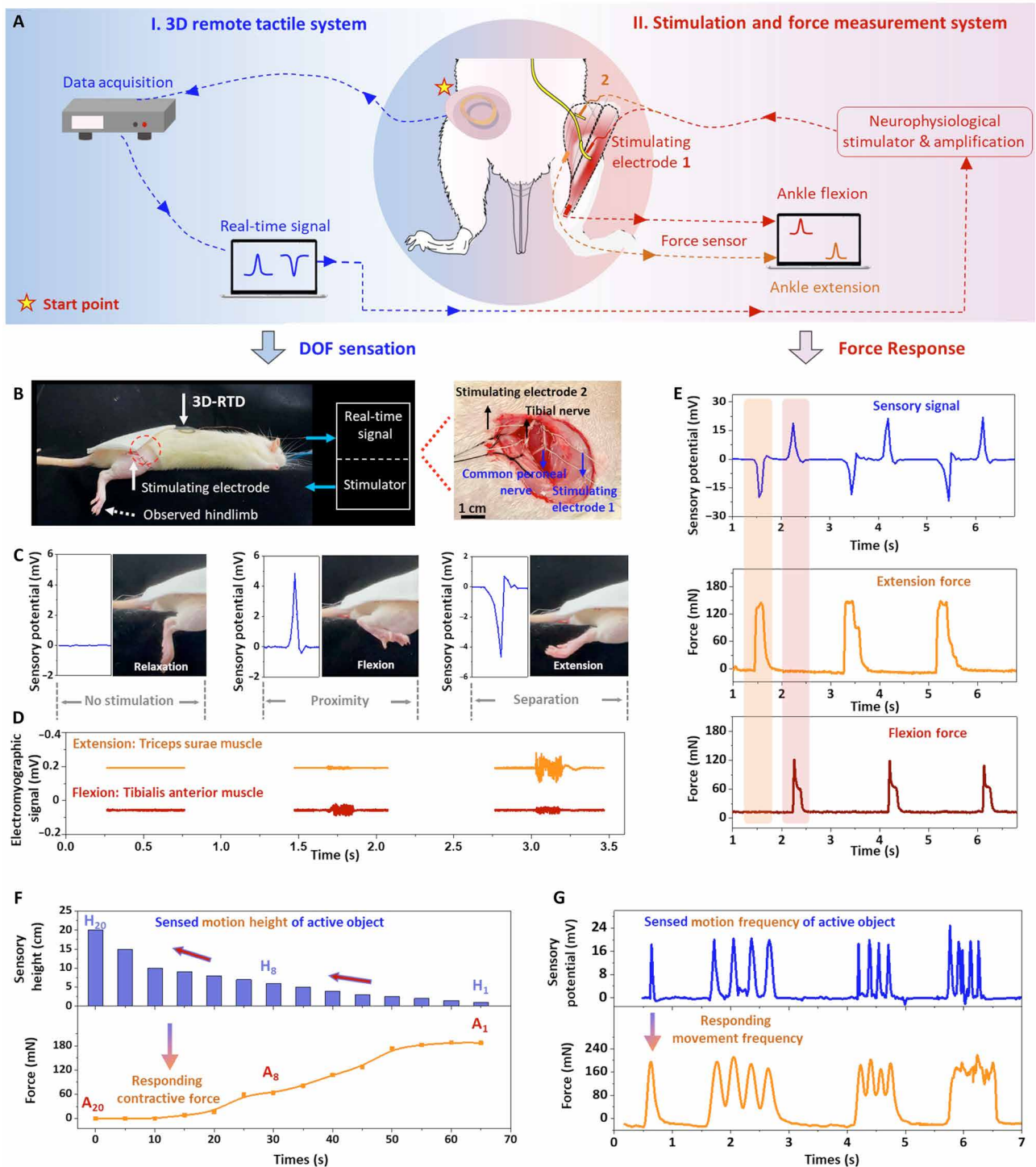
Fig. 3. Artificial 3D-TDS integrated into a neuromuscular system. (**A**) Schematic illustrations of system I, 3D-RTS: the acquisition of DOF mechanical motion with 3D-RTD attached on the back of the rat; system II, stimulation and force measurement system: the sensory potential from system I is synchronously transmitted to a neurophysiological stimulator with amplification. The positive signal is transferred to stimulating electrode 1 to excite the tibialis anterior muscle of the rat; the negative signal is transferred to stimulating electrode 2 to excite the triceps surae muscle. (**B**) Digital image of experimental conditions for the rat: the stimulating electrodes 1 and 2 connected with the common peroneal nerve and the tibial nerve, separately. (**C**) Relationship between sensory signals and responded foot positions synchronously obtained from a live rat, with no stimulation and no response (zero), object proximity and ankle flexion (+), and object separation and ankle extension (−), respectively. (**D**) Relationship between the corresponding EMG signals under the above three conditions. (**E**) Continuous signal profiles to show the relationship between the sensory potential and responded extension or flexion muscle contractive force of the hindlimb. (**F** and **G**) Quantification of force responses corresponding to the motion heights and frequencies of the active object.

separately to stimulating electrodes 1 and 2 in system II, leading to the movement of antagonistic muscles of the rat's hindlimb. As a result, the motion modes of the active object can be logically and quantitatively characterized through system I with sensory potential signs and through system II with synchronous muscle contractive manners and forces.

As presented in Fig. 3B, the two stimulating electrodes are separately connected to the common peroneal nerve and tibial nerve, which control the tibialis anterior muscle and triceps surae muscle of the rat hindlimb, respectively. For this reason, the external motion–generated V_{PRE} could be instantaneously used to power the hindlimb movement of the rat when 3D-RTD is stimulated by an active object. As shown in Fig. 3C, the rat hindlimb is naturally relaxed when there is no external stimulation. Then, the logical sensation is visually verified by the movement of the rat's ankle, where flexion corresponds to the proximity of an active object with a positive V_{PER} sign, and extension corresponds to the separation (movie S2). The synchronous electromyographic (EMG) signals are also recorded (Fig. 3D), under the same condition as that of Fig. 3C to confirm muscular activation with the artificial system. In the stimulation of object proximity, strong EMG signals from the tibialis anterior muscle are observed in ankle flexion, with simultaneous weak signals from the triceps surae muscle due to its antagonistic role. On the contrary, EMG signals of the triceps surae muscle are much stronger in ankle extension.

Likewise, the proximity-separation motion of the active object can be visibly distinguished by the activation of different muscular regions, in the case of cyclic stimulation (Fig. 3E). The intensity of the sensed stimulation can be directly correlated with the measured muscular contractive force. The effect of motion height and frequency of the active object is presented in Fig. 3 (F and G). The closer the active object is moving to the surface of the 3D-RTD, the stronger is the muscular contraction (movie S3). The frequency of muscle contraction also correlates and responds well to the frequency of the stimulation (movie S4 and fig. S21). However, for high sensory frequency, the muscle only performs incomplete contraction-relaxation cycles, with the wave trough of force increasing with frequency. To the high-frequency limit, tetanic contraction occurs when the value of stimulation reaches ~5 Hz, where the contraction force obtains a relatively stable value for a period of time. The 3D-RTD is efficient for seamless, reliable, and self-power signal transferring, from diverse DOF mechanical motions of an active object through the 3D-RTS to the biological motor system.

Obstacle avoidance with 3D-RTS

To demonstrate the capability of our 3D-RTS in sensation-interaction augmentation, a brain activity–related obstacle-avoidance scenario is presented here. Individuals in dim environments or with visual impairment are at high risk of collisions and falls. As presented in Fig. 4A, the traditional assistance for mobility guidance like long crutches still has limitations: They can only detect accessible obstacles on the ground with indispensable contact. The dangers above the ground are easily missed, and the collision risks could not be completely eliminated. From another point, such people are more likely to develop perceptual skills/maps to noncontact objects around them. Consequently, it is important to augment their perception to the outside world with the aid of artificial devices.

Here, we present a scenario of a rat with 3D-RTD as a neural interface patch on its back and stimulating electrodes in its right hindlimb, walking in dim environment, where the external stimulating obstacle of a 10 cm–by–10 cm PVDF film is hung from the ceiling of a platform (Fig. 4, B and C, and fig. S22). When the rat passes by the preestablished obstacle, it will perceive the "danger" and react via sensory feedback with brain-determined action and motor feedback with gait changes. First, DOF sensation–evoked brain activities are characterized through recording somatosensory evoked potential (SEP) in the hindlimb somatosensory cortex (Fig. 4D). The starting point of stimulation begins from 0 s, and the data in the first 0.25 s are excluded because of the stimulation artifact. Then, repeatable local field potential (LFP) responding to 3D stimulation is observed on the timeline with a mean value of 0.53 s and SD of 0.14 s in the same channel of eight trials. Meanwhile, the spikes are also extracted from the trough of LFP (fig. S23), indicating the reproducible neural activities in the hindlimb somatosensory cortex.

When the rat is passing the overhead obstacle, it will detect the potential danger via the patch, with sensed signals synchronously transmitting to its hindlimb (movie S5). Meanwhile, neural circuitry makes the rat conscious with a short pause and slight turnaround, indicating a sensation-perception-interaction process. Stimulation offered a warning to the rat's neural system, without exceeding a threshold for avoidance. Afterward, the gaits changing with incomplete print area and increased swing speed visually and quantitatively reflect the perception (Fig. 4, E and F). Therefore, 3D-RTS effectively activates microscopic neural signal through 3D-RTD responding to external motion of a noncontact object and then evokes perception and motor feedback, which is suitable for being integrated into the sensory-motor functionality of both organisms and cyborg.

DISCUSSION

In summary, we have demonstrated a stretchable self-powered 3D-RTD, which is capable of recognizing DOF motions of an active object in a 3D space based on its conductive-dielectric heterogeneous structure. It can logically identify the proximity-separation motion, with distance up to 20 cm and frequency from 0.0625 to 5 Hz. The related mechanism is revealed on the basis of the electrostatic theory and COMSOL finite element analysis, and the sensory performance is optimized accordingly via regulating the dielectric constant of heterogeneous materials. On the basis of the character of 3D-RTD in signal transmission and connection as a virtual synapse, the future objective that we are working toward is to intensively study the mechanism of conductive-dielectric heterostructure interaction and achieve more functions closer to that of the true synapse. The feasibility of 3D-RTD as a neuromorphic device is validated by constructing an artificial-biological integrated tactile system, synergistically realizing both microscale interaction between virtual and biological synaptic electron/ion and macroscopic interaction between external DOF mechanical motion and rat motor feedback. Furthermore, the practical application of 3D-RTD as a neural interface patch for sensory substitute and perceptual augmentation is verified in an obstacle-avoidance scenario, where the rat equipped with the device shows a sensation-perception-interaction neural process. Both the device and hybrid system present high sensory accuracy, making the device particularly desirable for security of interaction. It is expected that the 3D-RTD is complementary to the biological tactile sensation and can significantly augment its modalities. This device can be easily integrated and cost-effectively mass-produced via digital printing, which is a great progress for HI-AI
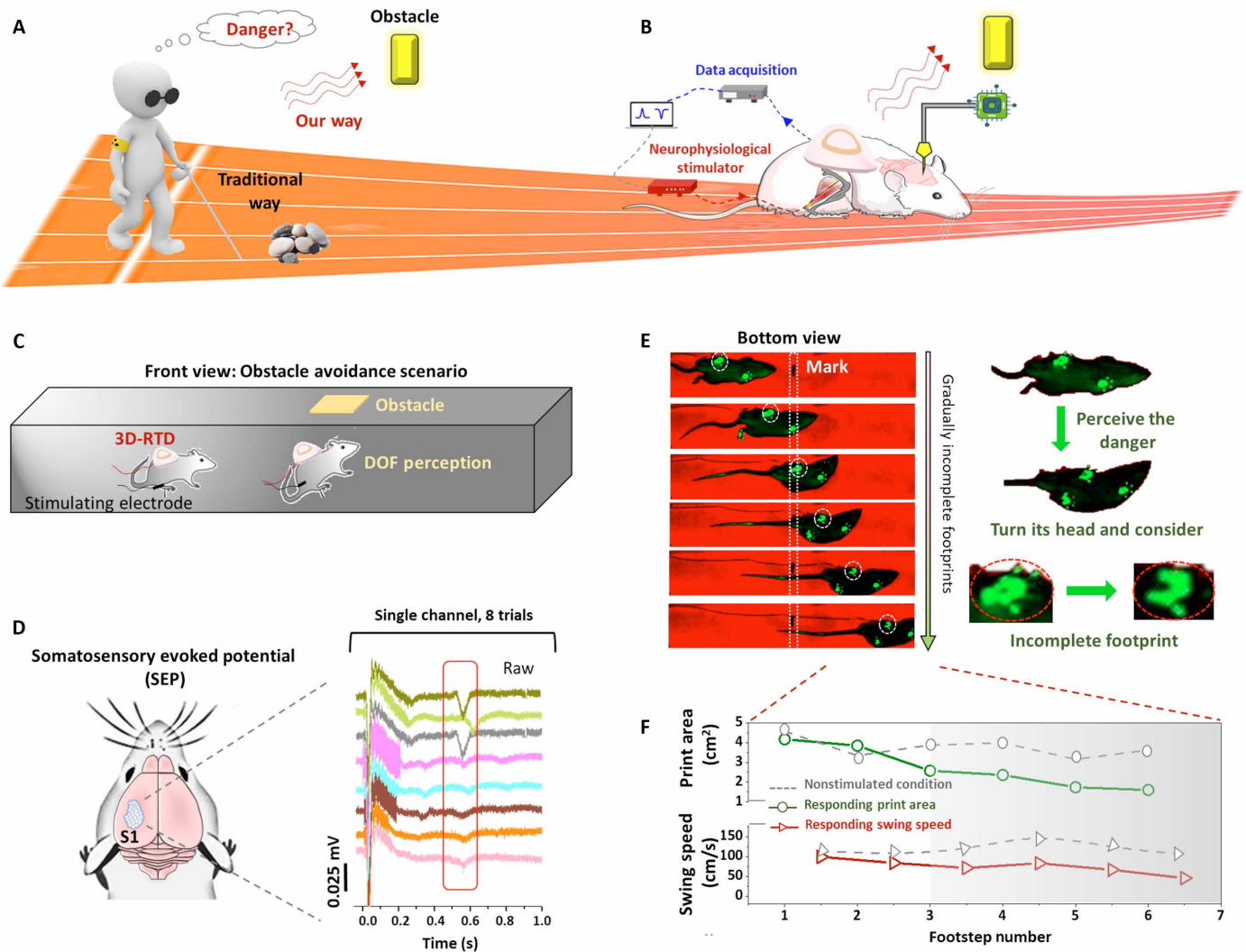
Fig. 4. Application of obstacle avoidance based on 3D-RTS. Schematic illustration: (**A**) Comparison of traditional and our way in obstacle avoidance for the blind, (**B**) to verify the feasibility of 3D-RTD in DOF perception via brain activity and motor feedback. (**C**) The front-view schematic of experimental scene: a rat running in the dim platform. (**D**) Record of poststimulus somatosensory evoked potential (SEP): raw traces from a single channel with eight trials. (**E**) The bottom-view digital images of the platform with real-time footprint of the target rat, where the black mark shows the position of obstacle. The larger version shows comparison of normal/abnormal rat body direction and complete/incomplete footprint. (**F**) Quantitative results of gait analysis: print area and swing speed. The gray shadow area represents entering and after the sensation.

interaction and augmentation. The proposed concept can further facilitate the development of a range of applications, especially in the field of interaction based on brain-like and hybrid intelligence.

MATERIALS AND METHODS
Materials and fabrication of 3D-RTD
First, the dielectric polymer EVA was prepared by dissolving EVA powder (28-25 EVA, ARKEMA) in dichloromethane (CH_2Cl_2) solvent and stirring for 4 hours with a rate of 360 rpm at 80°C. Once a uniform EVA solution was formed, BTO nanoparticles (30 nm of average particle size, Aladdin) were blended in ultrasonication bath at room temperature for 1 hour with a loading of 0, 4, 8, 12, and 16 weight %, respectively. Then, the EVA/BTO solution was cast into a film shape on an ultraflat glass surface. CH_2Cl_2 could be removed by natural evaporation in a fuming cupboard for 8 hours.

As for 3D-RTD, the fabricated EVA/BTO nanocomposite film with a controlled thickness of 130 μm was cut into a wafer shape with a diameter of 3 cm. Then, the ring-shaped Au layer as the electrode was magnetron sputtered (Magnetron Sputtering Machine, TWS-300) onto the lower surface of the EVA/BTO film with the help of mask template, of which the sputtering thickness was 1.7 to 2 nm/s, and the sputtering time was 15 s. The cross section of two-layered structure was characterized via scanning electron microscopy (Phenom Pharos) as illustrated in Fig. 2A.

Construction of hybrid neuromuscular system
System I. 3D-RTS
The 3D-RTD was attached onto the back surface of a rat as shown in the left side of fig. S18, and the sensory potential signals stimulated by an external active object were collected using the Agilent 34411A Digit Multimeter. The Agilent multimeter can execute

50,000 readings, at most, per second when a trigger is initiated. The undesired signal frequency components such as 50 Hz of power frequency signals have been rejected through the Agilent multimeter, with its built-in noise-rejection function. Then, the acquired sensory signals were displayed using the LabVIEW software (National Instruments, USA) with simultaneous recording (figs. S19 and S20).

System II. Stimulation and force measurement system
In addition, as shown in fig. S18, the sensory signal from the left system was collected via LabVIEW software, where the V_{PER} was amplified using a digital amplifier with a voltage gain of 10; then, it was synchronously output to a neurophysiological stimulator (Master-9, A.M.P.I., Israel) in the right side. Two stimulating electrodes, regarded as sensory output electrodes, were used to connect Master 9 and the motor nerves of the rat hindlimb. When 3D-RTD was operated by DOF motion of an active object, the output electric potential would flow through the left 3D-RTS to the right force measurement system, and the stimulated muscular contractive forces of the rat hindlimb could be acquired simultaneously.

Finite element simulation
Finite element simulations were performed on the basis of the Gauss theorem of static electricity field and dielectric electric field, using a COMSOL Multiphysics software package. When a dielectric is present in an electric field, the electric field strength is equal to the superposition of the field excited by the free charge ρ_0 and the polarized charge ρ_e

$$\nabla \cdot \vec{E}(\vec{r}) = \frac{\rho_0 + \rho_p}{\varepsilon_0} \ \rightarrow \ \nabla \cdot (\varepsilon_0 \vec{E} + \vec{P}) = \rho_e \tag{2}$$

where $\vec{E}$ is the intensity of external electric field, $\vec{P}$ is the electric polarization intensity, and ε_0 is the vacuum dielectric constant. Then, define $\vec{D} = \varepsilon_0\vec{E} + \vec{P}$ as the electric displacement vector of the dielectric, and $\vec{D} = \varepsilon_0\vec{E}$ when there is no dielectric under the vacuum condition. In the presence of a dielectric, because both $\vec{D}$ and $\vec{P}$ are the function of $\vec{E}$, the electric displacement vector could be obtained as

$$\vec{D} = \varepsilon\vec{E} = \varepsilon_0\varepsilon\vec{E} \tag{3}$$

where ε_r is the relative dielectric constant. Under the condition of 2D space, the steady-state study of electrostatic field governing equation $\vec{E} = -\nabla V$ is adopted, and the boundary conditions for charge conservation

$$\nabla \cdot (\varepsilon_0\varepsilon\vec{E}) = \rho_v \tag{4}$$

are used here, where V is the electric potential and ρ is charge density.

Animal experiment
Implantation of stimulating electrodes connected to sensory device
As described above, one end of the stimulating electrodes was connected to the Master 9 neurophysiological stimulator, and the other end is linked to the tibial and the common peroneal nerve of the rat hindlimb, separately (Fig. 3A). In addition, as illustrated in Fig. 3B, the front end of the stimulating electrode wire (catalog no. 793500, Omentic, USA) was shaped like a hook to easily and firmly hook the target nerve. Meanwhile, the stimulating electrode wires were fixed to the adjacent muscle with 0-8 nylon surgical suture to prevent shedding.

Recording of EMG signals
The EMG signal recording was performed by the High-Performance and High-Density Acquisition System of Neuromuscular Electrophysiological Signals (NES-64B01, Research Center for Neural Engineering, Shenzhen Institute of Advanced Technology, Chinese Academy of Science, China), which is capable of executing multichannel biological signal acquisition. The electrode was placed on the triceps surae/tibialis anterior muscle of the hindlimb, and the reference electrode was inserted under the skin of the tail. The final output was connected to an analog-to-digital converter board with a sampling frequency of 2 kHz. Then, the acquired neural signal was simultaneously recorded using the Biopotential Sensation Software (homemade software), with a band-pass filter (20 to 500 Hz) and a notch filter (50 Hz) to remove interfering signals.

Recording of SEP in somatosensory cortex
Before the experiment, the head of an anesthetized rat was fixed in a stereoscopic fixator, followed by removing the scalp, subcutaneous tissue, and skull; then, the sensory cortex of the lower extremities was exposed (position: anteroposterior, 0.36 to 2.28 mm; mediolateral, 2.8 to 3.6 mm). The entire surface of the rat skull was sealed with a dental cement ring to form a closed groove, and a 32-channel neural electrode (LOTUS BIOCHIPS, ASSY-37.1-2.1) was inserted into the left hindlimb somatosensory cortex of the rat to record SEP. A small amount of normal saline was filled into the closed dental cement groove, where the reference electrode was placed in. The recording end of the electrode was connected to the neural signal recording system (Intan RHD Recording Controller, 512 ch), of which the signal sampling rate was 20 kHz. The DOF stimuli were repeatedly performed and then delivered through 3D-RTD to the sciatic nerve of the rat, and the SEP of the somatosensory cortex was sampled, with multiple trials. During the recording, isofluorane concentration is kept at 1.5% to maintain the depth of anesthesia, keeping the rat in the second stage of sleep; meanwhile, the anesthesia status was assessed by observing the electrocardiograph.

Data analysis of SEP
A digital 50-Hz notch filter was used to reduce power frequency interference, a digital 80- to 300-Hz band-pass filter (MATLAB, MathWorks, Natick, MA) was used to extract LFP, and a digital high-pass filter (600-Hz cutoff, fourth-order Butterworth; MATLAB) was used to extract the high-frequency components of the stimulation-evoked neural signal. The mean value and SD were calculated by extracting the SEP of eight trials and corresponding 32 channels. Parameters of neural activity–related spikes were offline extracted through Offline Sorter (Plexon Inc.).

Acquisition of force response
First, the triceps muscle and tibialis anterior muscle of the rat hindlimb were partly separated from the body, of which the proximal tendons were retained on the tibia, and the distal tendons were dissected, respectively. Then, the target tendons were connected to the mechanical sensor of force detection instrument (biological signal acquisition and processing system, Medlab-U/8C502, Nanjing Meiyi Technology Co. Ltd.; mechanical sensors, JZ101 tension transducer, range of 0 to 50 g, no. 5580, Beijing Xinhangxing Technology & Trade Co. Ltd.) through 0-4 nylon surgical suture. During the test, the pulley and ligation line of the target muscle were kept at the same level, and the tension transducer was connected to the input end of the acquisition system for data collection. The two muscles contracted separately in response to sensation of proximity and separation stimulation of an external active object (Fig. 3E).

Gait analysis

The sensory states of the walking rat were characterized by gait analysis via animal gait analysis system (T60101, Shenzhen Zhong Shi Scientific Instrument Co. Ltd.), with the parameters of print area and swing speed. The print area is defined as the total area of a complete footprint, at least as large as the maximum contact area. The swing speed is defined as the speed at which a foot moves and can be expressed as swing speed = stride length/swing (unit distance per second). Before the formal experiment, the rat had been trained for a week to familiarize themselves with the 1-m-long track. During the test, the sensory device is stuck to the back of the rat, and the stimulating electrodes are connected to their sciatic nerves. After the rat was placed at the entrance of the track, it would run to the track exit of its own accord and would perceive the existence of a noncontact object hanging in the middle of the track. All procedures were approved by the Animal Research Committee of Shenzhen Institutes of Advanced Technology, Chinese Academy of Sciences (approval no. LLSQ2110290003).

SUPPLEMENTARY MATERIALS

Supplementary material for this article is available at https://science.org/doi/10.1126/sciadv.abo5314

View/request a protocol for this paper from *Bio-protocol*.

REFERENCES AND NOTES

1. P. Delmas, J. Hao, L. Rodat-Despoix, Molecular mechanisms of mechanotransduction in mammalian sensory neurons. *Nat. Rev. Neurosci.* **12**, 139–153 (2011).
2. Q. Zhang, S. Hu, R. Talay, Z. Xiao, D. Rosenberg, Y. Liu, G. Sun, A. Li, B. Caravan, A. Singh, A prototype closed-loop brain-machine interface for the study and treatment of pain. *Nat. Biomed. Eng.* 10.1038/s41551-021-00736-7 (2021).
3. S. Chun, J.-S. Kim, Y. Yoo, Y. Choi, S. J. Jung, D. Jang, G. Lee, K.-I. Song, K. S. Nam, I. Youn, D. Son, C. Pang, Y. Jeong, H. Jung, Y.-J. Kim, B.-D. Choi, J. Kim, S.-P. Kim, W. Park, S. Park, An artificial neural tactile sensing system. *Nat. Electron.* **4**, 429–438 (2021).
4. Y. Kim, A. Chortos, W. Xu, Y. Liu, J. Y. Oh, D. Son, J. Kang, A. M. Foudeh, C. Zhu, Y. Lee, S. Niu, J. Liu, R. Pfattner, Z. Bao, T.-W. Lee, A bioinspired flexible organic artificial afferent nerve. *Science* **360**, 998–1003 (2018).
5. H. Kim, J. Choi, K. K. Kim, P. Won, S. Hong, S. H. Ko, Biomimetic chameleon soft robot with artificial crypsis and disruptive coloration skin. *Nat. Commun.* **12**, 4658 (2021).
6. T. Someya, Z. Bao, G. G. Malliaras, The rise of plastic bioelectronics. *Nature* **540**, 379–385 (2016).
7. R. Green, M. R. Abidian, Conducting polymers for neural prosthetic and neural interface applications. *Adv. Mater.* **27**, 7620–7637 (2015).
8. G. Chen, Y. Li, M. Bick, J. Chen, Smart textiles for electricity generation. *Chem. Rev.* **120**, 3668–3720 (2020).
9. J. C. Yang, J. Mun, S. Y. Kwon, S. Park, Z. Bao, S. Park, Electronic skin: Recent progress and future prospects for skin-attachable devices for health monitoring, robotics, and prosthetics. *Adv. Mater.* **31**, 1904765 (2019).
10. Y. van de Burgt, E. Lubberman, E. J. Fuller, S. T. Keene, G. C. Faria, S. Agarwal, M. J. Marinella, A. A. Talin, A. Salleo, A non-volatile organic electrochemical device as a low-voltage artificial synapse for neuromorphic computing. *Nat. Mater.* **16**, 414–418 (2017).
11. Y. Wu, Y. Liu, Y. Zhou, Q. Man, C. Hu, W. Asghar, F. Li, Z. Yu, J. Shang, G. Liu, M. Liao, R.-W. Li, A skin-inspired tactile sensor for smart prosthetics. *Sci. Robot.* **3**, eaat0429 (2018).
12. Y. H. Jung, B. Park, J. U. Kim, T.-i. Kim, Bioinspired electronics for artificial sensory systems. *Adv. Mater.* **31**, 1803637 (2019).
13. Y. Lee, J. Y. Oh, W. Xu, O. Kim, T. R. Kim, J. Kang, Y. Kim, D. Son, J. B.-H. Tok, M. J. Park, Z. Bao, T.-W. Lee, Stretchable organic optoelectronic sensorimotor synapse. *Sci. Adv.* **4**, eaat7387 (2018).
14. H. Guo, X. Pu, J. Chen, Y. Meng, M.-H. Yeh, G. Liu, Q. Tang, B. Chen, D. Liu, S. Qi, C. Wu, C. Hu, J. Wang, Z. L. Wang, A highly sensitive, self-powered triboelectric auditory sensor for social robotics and hearing aids. *Sci. Robot.* **3**, eaat2516 (2018).
15. J. Yeom, A. Choe, S. Lim, Y. Lee, S. Na, H. Ko, Soft and ion-conducting hydrogel artificial tongue for astringency perception. *Sci. Adv.* **6**, eaba5785 (2020).
16. N. Imam, T. A. Cleland, Rapid online learning and robust recall in a neuromorphic olfactory circuit. *Nat. Mach. Intell.* **2**, 181–191 (2020).
17. B. C.-K. Tee, A. Chortos, A. Berndt, A. K. Nguyen, A. Tom, A. McGuire, Z. C. Lin, K. Tien, W.-G. Bae, H. Wang, P. Mei, H.-H. Chou, B. Cui, K. Deisseroth, T. N. Ng, Z. Bao, A skin-inspired organic digital mechanoreceptor. *Science* **350**, 313–316 (2015).
18. C. Wang, D. Hwang, Z. Yu, K. Takei, J. Park, T. Chen, B. Ma, A. Javey, User-interactive electronic skin for instantaneous pressure visualization. *Nat. Mater.* **12**, 899–904 (2013).
19. D. J. Lipomi, M. Vosgueritchian, B. C. K. Tee, S. L. Hellstrom, J. A. Lee, C. H. Fox, Z. Bao, Skin-like pressure and strain sensors based on transparent elastic films of carbon nanotubes. *Nat. Nanotechnol.* **6**, 788–792 (2011).
20. T. Bu, T. Xiao, Z. Yang, G. Liu, X. Fu, J. Nie, T. Guo, Y. Pang, J. Zhao, F. Xi, C. Zhang, Z. L. Wang, Stretchable triboelectric–photonic smart skin for tactile and gesture sensing. *Adv. Mater.* **30**, 1800066 (2018).
21. H. Han, H. Yu, H. Wei, J. Gong, W. Xu, Recent progress in three-terminal artificial synapses: From device to system. *Small* **15**, 1900695 (2019).
22. M. Prezioso, F. Merrikh-Bayat, B. D. Hoskins, G. C. Adam, K. K. Likharev, D. B. Strukov, Training and operation of an integrated neuromorphic network based on metal-oxide memristors. *Nature* **521**, 61–64 (2015).
23. X. Yu, Z. Xie, Y. Yu, J. Lee, A. Vazquez-Guardado, H. Luan, J. Ruban, X. Ning, A. Akhtar, D. Li, B. Ji, Y. Liu, R. Sun, J. Cao, Q. Huo, Y. Zhong, C. Lee, S. Kim, P. Gutruf, C. Zhang, Y. Xue, Q. Guo, A. Chempakasseril, P. Tian, W. Lu, J. Jeong, Y. Yu, J. Cornman, C. Tan, B. Kim, K. Lee, X. Feng, Y. Huang, J. A. Rogers, Skin-integrated wireless haptic interfaces for virtual and augmented reality. *Nature* **575**, 473–479 (2019).
24. J. Yu, X. Yang, G. Gao, Y. Xiong, Y. Wang, J. Han, Y. Chen, H. Zhang, Q. Sun, Z. L. Wang, Bioinspired mechano-photonic artificial synapse based on graphene/MoS$_2$ heterostructure. *Sci. Adv.* **7**, eabd9117 (2021).
25. S. C. B. Mannsfeld, B. C. K. Tee, R. M. Stoltenberg, C. V. H. H. Chen, S. Barman, B. V. O. Muir, A. N. Sokolov, C. Reese, Z. Bao, Highly sensitive flexible pressure sensors with microstructured rubber dielectric layers. *Nat. Mater.* **9**, 859–864 (2010).
26. X. Qu, W. Niu, R. Wang, Z. Li, Y. Guo, X. Liu, J. Sun, Solid-state and liquid-free elastomeric ionic conductors with autonomous self-healing ability. *Mater. Horiz.* **7**, 2994–3004 (2020).
27. Y. S. Zhou, G. Zhu, S. Niu, Y. Liu, P. Bai, Q. Jing, Z. L. Wang, Nanometer resolution self-powered static and dynamic motion sensor based on micro-grated triboelectrification. *Adv. Mater.* **26**, 1719–1724 (2014).
28. J. Yu, G. Gao, J. Huang, X. Yang, J. Han, H. Zhang, Y. Chen, C. Zhao, Q. Sun, Z. L. Wang, Contact-electrification-activated artificial afferents at femtojoule energy. *Nat. Commun.* **12**, 1581 (2021).
29. W. Seung, H. J. Yoon, T. Y. Kim, H. Ryu, J. Kim, J. H. Lee, J. H. Lee, S. Kim, Y. K. Park, Y. J. Park, S.-W. Kim, Boosting power-generating performance of triboelectric nanogenerators via artificial control of ferroelectric polarization and dielectric properties. *Adv. Energy Mater.* **7**, 1600988 (2017).
30. R. Yang, Y. Qin, L. Dai, Z. L. Wang, Power generation with laterally packaged piezoelectric fine wires. *Nat. Nanotechnol.* **4**, 34–39 (2009).
31. Z. L. Wang, J. Chen, L. Lin, Progress in triboelectric nanogenerators as a new energy technology and self-powered sensors. *Energ. Environ. Sci.* **8**, 2250–2282 (2015).
32. J. Wang, L. Pan, H. Guo, B. Zhang, R. Zhang, Z. Wu, C. Wu, L. Yang, R. Liao, Z. L. Wang, Rational structure optimized hybrid nanogenerator for highly efficient water wave energy harvesting. *Adv. Energy Mater.* **9**, 1802892 (2019).
33. M. Kaltenbrunner, T. Sekitani, J. Reeder, T. Yokota, K. Kuribara, T. Tokuhara, M. Drack, R. Schwödiauer, I. Graz, S. Bauer-Gogonea, S. Bauer, T. Someya, An ultra-lightweight design for imperceptible plastic electronics. *Nature* **499**, 458–463 (2013).
34. M. Norgia, A. Pesatori, F. Cavedo, paper presented at the 2018 IEEE International Instrumentation and Measurement Technology Conference (I2MTC), Houston, TX, 14 to 17 May 2018.
35. O. Ulori, M. M. Igwele, R. E. Ombu, A design perspective of an IR beam barrier and proximity detector. *Financial Eng. Risk Manage.* **1**, 1–10 (2019).
36. D. F. Q. Melo, B. M. C. Silva, N. Pombo, L. Xu, Internet of things assisted monitoring using ultrasound-based gesture recognition contactless system. *IEEE Access* **9**, 90185–90194 (2021).
37. S. E. Navarro, S. Mühlbacher-Karrer, H. Alagi, H. Zangl, K. Koyama, B. Hein, C. Duriez, J. Smith, Proximity perception in human-centered robotics: A survey on sensing systems and applications. *IEEE Trans. Robot.* **38**, 1599–1620 (2021).
38. L. Lu, C. Jiang, G. Hu, J. Liu, B. Yang, Flexible noncontact sensing for human-machine interaction. *Adv. Mater.* **33**, 2100218 (2021).
39. L. Ding, Y. Wang, C. Sun, Q. Shu, T. Hu, S. Xuan, X. Gong, Three-dimensional structured dual-mode flexible sensors for highly sensitive tactile perception and noncontact sensing. *ACS Appl. Mater. Interfaces* **12**, 20955–20964 (2020).
40. D. V. Anaya, K. Zhan, L. Tao, C. Lee, M. R. Yuce, T. Alan, Contactless tracking of humans using non-contact triboelectric sensing technology: Enabling new assistive applications for the elderly and the visually impaired. *Nano Energy* **90**, 106486 (2021).
41. Z. L. Wang, Triboelectric nanogenerators as new energy technology for self-powered systems and as active mechanical and chemical sensors. *ACS Nano* **7**, 9533–9557 (2013).

42. Y. Tang, H. Zhou, X. Sun, N. Diao, J. Wang, B. Zhang, C. Qin, E. Liang, Y. Mao, Triboelectric touch-free screen sensor for noncontact gesture recognizing. *Adv. Funct. Mater.* **30**, 1907893 (2020).

43. P. Rokita, Generating depth of-field effects in virtual reality applications. *IEEE Comput. Grap. Appl.* **16**, 18–21 (1996).

44. O. Fujiwara, M. Okazaki, T. Azakami, Electrification properties of human body for walking-motion. *Electron. Commun. Jpn.* **74**, 99–107 (1991).

45. E. N. Jayaweera, K. R. Wijewardhana, T. K. Ekanayaka, A. Shahzad, J.-K. Song, Triboelectric nanogenerator based on human hair. *ACS Sustain. Chem. Eng.* **6**, 6321–6327 (2018).

46. R. Elsdon, F. R. G. Mitchell, Contact electrification of polymers. *J. Phys. D Appl. Phys.* **9**, 1445–1460 (1976).

47. F. Sun, Q. Lu, S. Feng, T. Zhang, Flexible artificial sensory systems based on neuromorphic devices. *ACS Nano* **15**, 3875–3899 (2021).

48. M. Zhang, Z. Tang, X. Liu, J. Van der Spiegel, Electronic neural interfaces. *Nat. Electron.* **3**, 191–200 (2020).

49. B. Chen, Y. Cao, Q. Li, Z. Yan, R. Liu, Y. Zhao, X. Zhang, M. Wu, Y. Qin, C. Sun, W. Yao, Z. Cao, P. M. Ajayan, M. O. L. Chee, P. Dong, Z. Li, J. Shen, M. Ye, Liquid metal-tailored gluten network for protein-based e-skin. *Nat. Commun.* **13**, 1206 (2022).

50. V. Arumugam, M. D. Naresh, R. Sanjeevi, Effect of strain rate on the fracture behaviour of skin. *J. Biosci.* **19**, 307–313 (1994).

51. W. Gough, How thick is the charge layer on a metallic surface? *Phys. Educ.* **21**, 81–82 (1986).

52. H. C. Ohanian, On the approach to electro- and magneto-static equilibrium. *Am. J. Phys.* **51**, 1020–1022 (1983).

53. J. Luo, Z. L. Wang, Recent progress of triboelectric nanogenerators: From fundamental theory to practical applications. *EcoMat* **2**, e12059 (2020).

54. D. R. Wolters, J. J. van der Schoot, Kinetics of charge trapping in dielectrics. *J. Appl. Phys.* **58**, 831–837 (1985).

55. C. Wang, M. Liu, M. Thijs, F. G. B. Ooms, S. Ganapathy, M. Wagemaker, High dielectric barium titanate porous scaffold for efficient Li metal cycling in anode-free cells. *Nat. Commun.* **12**, 6536 (2021).

56. K. Y. Lee, S. K. Kim, J.-H. Lee, D. Seol, M. K. Gupta, Y. Kim, S.-W. Kim, Controllable charge transfer by ferroelectric polarization mediated triboelectricity. *Adv. Funct. Mater.* **26**, 3067–3073 (2016).

57. Y. Shi, F. Wang, J. Tian, S. Li, E. Fu, J. Nie, R. Lei, Y. Ding, X. Chen, Z. L. Wang, Self-powered electro-tactile system for virtual tactile experiences. *Sci. Adv.* **7**, eabe2943 (2021).

Science Advances

An artificial remote tactile device with 3D depth-of-field sensation

Shanshan ZhuYuanheng LiHuoerhute YelemulatiXinping DengYongcheng LiJingjing WangXiaojian LiGuanglin LiPaschalis GkoupidenisYanlong Tai

View the article online
https://www.science.org/doi/10.1126/sciadv.abo5314
Permissions
https://www.science.org/help/reprints-and-permissions